PAPER

Direct visualization of particle attachment to a pendant drop†

C. Li, J. A. Simmons, M. Moradiafrapoli and J. O. Marston*

An experimental investigation is carried out into the attachment of a single particle to a liquid drop. High-speed videography is used to directly visualize the so-called 'snap-in' effect which occurs rapidly over sub-millisecond timescales. Using high-magnification, the evolution of the contact line around the particle is tracked and dynamic features such as the contact angle, wetted radius and force are extracted from these images to help build a fundamental understanding of the process. By examining the wetted length in terms of an arc angle, ϕ, it is shown that the early wetting stage is an inertial-dominated process and best described by a power law relation, i.e. $\phi \sim (t/\tau)^{\alpha}$, where τ is an inertial timescale. For the subsequent lift-off stage, the initial particle displacement is matched with that predicted using a simple balance between particle weight and capillary force with reasonable agreement. The lift-off force is shown to be on the order of 1–100 μN, whilst the force of impacting droplets is known to be on the order of 10–1000 mN. This explains the ease in which liquid marbles are formed during impact experiments.

1 Introduction

Particle-laden interfaces (PLIs) are of fundamental interest due to their commonplace occurrence in both nature and industry.[1–4] Determining properties and stability of PLIs has been the subject of intensive research over the past decade with significant emphasis on the relationship between mechanical strength, elasticity and particle structure and density at the interface.[5–8] A specific sub-class of PLIs are liquid marbles, whereby liquid droplets are coated with a shell of hydrophobic particles.[3,9,10] Liquid marbles possess some interesting properties such as divisibility[11] and longevity due to low evaporation rates.[12] One curious feature of liquid marbles and PLIs in general is that of arrested shapes, where the shape of the interface can become locked in an out-of-equilibrium (non-spherical) shape,[13–17] where the key mechanisms are not fully understood. Furthermore, the main attractive feature of liquid marbles is that they are mobile, therefore interfacial jamming may be undesirable.

An obvious prerequisite for PLIs is that the particle must attach to and remain at the free-surface of the liquid volume. The actual attachment stage is fundamental but has received relatively little attention[18–20] and so it is this specific process, referred to as the 'snap-in' effect, that will be the focus of this investigation.

Department of Chemical Engineering, Texas Tech University, Lubbock, TX 79409, USA. E-mail: Jeremy.Marston@ttu.edu
† Electronic supplementary information (ESI) available. See DOI: 10.1039/c6sm02495e

An overview of the general snap-in effect is shown in Fig. 1 for a glass bead with radius $r_p = 1$ mm and a pendant water droplet with a radius of curvature at the apex of $R = 2.7$ mm. After the very first contact of the particle with the interface, the initial dynamic wetting phase takes place as the three phase solid–liquid–gas contact line begins to advance around the particle. Once sufficient wetting has taken place, the particle is lifted off into the liquid phase. The particle then oscillates with the drop until an equilibrium configuration is reached.[18] The evolution of the contact line during the initial wetting phase as well as the force balance that governs the lift-off phase are key to this process and will be studied here.

Theoretically, the wettability of an ideal substrate is measured by the equilibrium contact angle θ_e. When the dynamic contact angle θ the angle measured through the liquid phase that the free surface makes with the solid substrate at the contact line, reaches the value of θ_e, the forces acting upon the contact line are in equilibrium and hence the contact line becomes pinned, as represented by Young's equation.[21] The contact angle is known to vary with changes in the contact line speed[22,23,41] and is therefore referred to as the dynamic contact angle. When $\theta > \theta_e$, the contact line advances and the liquid phase displaces the gas phase from the substrate in a process known as dynamic wetting. Conversely, when $\theta < \theta_e$, dynamic de-wetting takes place as the gas phase displaces the liquid phase from the substrate. The evolution of the dynamic contact angle, θ, during the initial wetting phase and the influence of substrate wettability on the entire snap-in effect will be examined here.
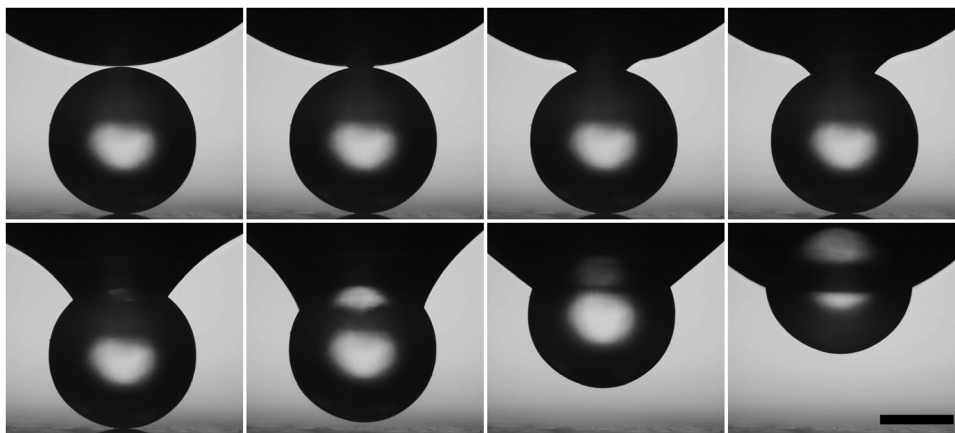
Fig. 1 Image sequence from a high-speed video showing the snap-in process of a glass bead with radius r_p = 1 mm into a pendant water droplet with droplet radius R = 2.7 mm. The scale bar in the final image is 1 mm long. Images are taken at times t = −10, 0, 0.5, 1, 3, 10, 20, and 30 ms from first contact. Lift-off occurs between images 5 and 6, at $t* \approx$ 4 ms.

A previous study assessed the snap-in force associated with the attachment of single particles to a water droplet using particles stuck to atomic force microscope (AFM) cantilevers.[18] Using both hydrophilic (small θ_e) and hydrophobic (large θ_e) glass beads with radii between 22 and 86 μm, a force on the order of micro-Newtons and snap-in time on the order of 0.1 milliseconds was accurately derived. Following the first contact, significant oscillation was observed before attaining an equilibrium position at the drop surface. This method of using AFM probes yields good spatial and temporal resolution of the particle position, however, the initial wetting of the particle was not addressed. Other recent works studying particle-induced capillary phenomenon include the attachment of a single particle to a pendant drop for expanding the applicability of pendant drop tensiometry[24] and the evaporation of a droplet about a single particle on a substrate.[25]

During the very initial stages of wetting, for example when a droplet is brought into contact with a flat, dry, solid surface, it has been reported that the contact line motion is dictated by a balance between capillary pressure, $\sim \sigma R/r^2$, and inertial pressure, $\sim \rho V_c^2 \approx \rho (dr/dt)^2$, where ρ and σ are the liquid density and surface tension, R is the droplet radius, r is the wetted radius and V_c is the contact line speed.[26] This balance leads to the scaling of the contact line radius, $r(t) \sim (\sigma R/\rho)^{1/4} t^{1/2}$, which assumes no viscous dissipation at the contact line and perfect wetting (i.e. $\theta_e \approx 0$) and is therefore similar to the bridge radius evolution in inviscid coalescence.[27–29] Subsequent assessment of the initial stages of drops contacting dry solid surfaces[30] found that the spreading is best described by $r/R = C(t/\tau)^\alpha$, where $\tau = (\rho R^3/\sigma)^{1/2}$ is the inertial-capillary timescale, and the prefactor, C, and exponent, α, are functions of θ_e. For high equilibrium contact angles $\theta_e > 100°$, the exponent $\alpha \approx 1/4$, whilst for low equilibrium contact angles $\theta_e \approx 3°$, the exponent $\alpha = 1/2$, recapturing the inviscid scaling law. Furthermore, the scaled data exhibited a cross-over time at $t/\tau \approx$ 2–3, corresponding to the transition from inertial to viscous spreading, at which point the spreading is described by Tanner's law with $r(t) \sim R(\sigma t/\mu R)^{1/10}$, with dynamic viscosity μ. Further evaluation of the spreading

dynamics found that the θ_e-dependence is not exhibited at very short timescales where $t/\tau = O(10^{-3}–10^{-1})$ and that contact line friction is also insignificant at such timescales.[31–33] Despite this wealth of literature, one factor that has been largely overlooked in the assessment of early-time dynamic wetting is the influence of substrate curvature.[34–36] This issue will also be considered herein.

2 Materials and methods

The experimental configuration used for the present study is shown schematically in Fig. 2(a). A single, isolated particle is placed onto a glass microscope slide on top of a labjack and brought into position directly underneath a pendant liquid droplet. The position is checked by two orthogonal camera views to ensure alignment prior to commencing the experiment. Once in position, a motorized translation stage (MTS50-Z8, Thorlabs Inc.), employing a DC servo motor, is used to lower the pendant droplet towards the particle at the lowest possible travel speed of 50 μm s^{-1}. As soon as the liquid is observed to contact the particle, the motion of the stage is stopped and the video is triggered.

The particles chosen were spherical glass beads (Cospheric LLC) with density ρ_p = 2500 kg m^{-3} and specified diameter ranges of 355–425 μm, 425–500 μm, 500–600 μm, 1 mm and 2 mm. The beads are cleaned by washing with acetone, then by immersion in ethanol and sonication in an ultrasonic bath for several minutes before a final DI water rinse. The beads are then dried on a hot plate.

The pendant droplet emanates from a glass tube with inner diameter of 2.6 mm and outer diameter of 5 mm. The radius of curvature, R, is measured from the video clips before contact occurs. The test liquids used were DI water, water–glycerol and water–ethanol mixtures, a 5 mole salt solution (NaCl, Sigma Aldrich) and a surfactant solution (SDS, Sigma Aldrich). The physical properties and equilibrium contact angles of these liquids are summarized in Table 1.

The equilibrium contact angle measurements were found by depositing a droplet of each liquid on a clean microscope slide,

(a)

(b)

(c)
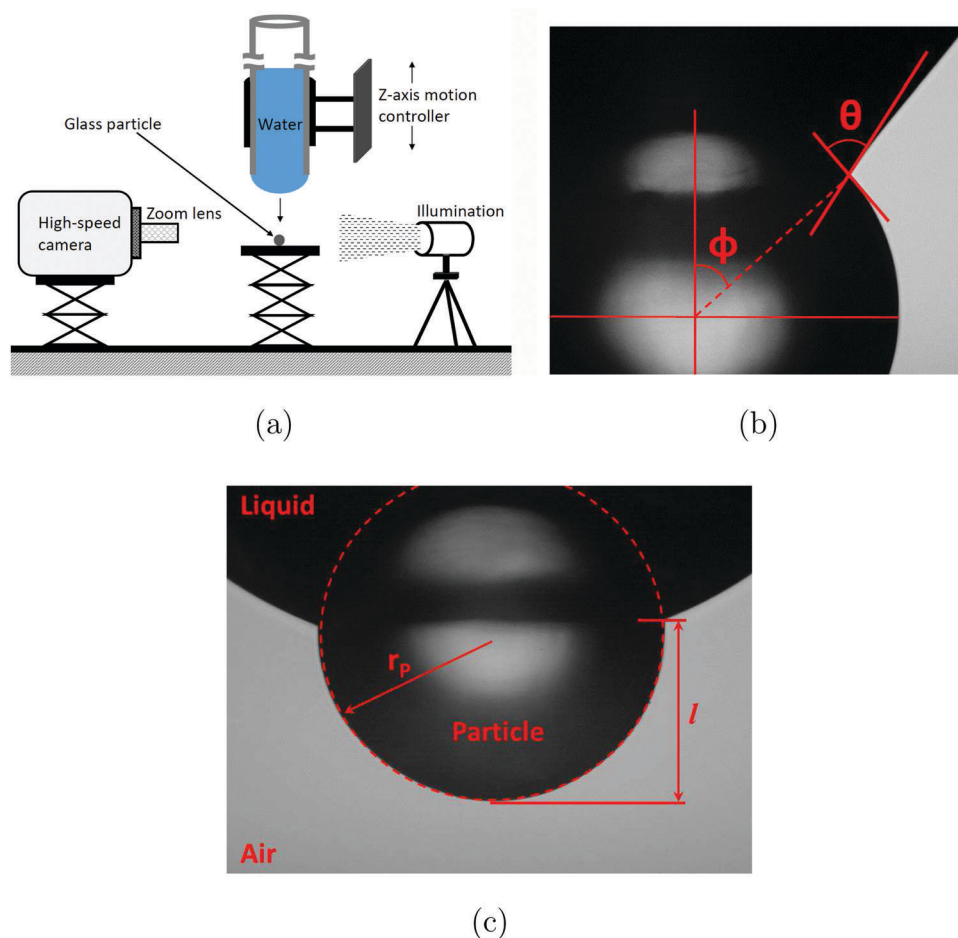
Fig. 2 (a) Schematic representation of the experimental setup used in the present study. (b) Graphical definition of the contact line position in terms of arc angle, ϕ and dynamic contact angle, θ. (c) Graphical definition of the protrusion length, l, of a particle at equilibrium.

prepared using the same cleaning procedure as for the particles. Additional tests with plasma-cleaned surfaces were performed to compare with the aforementioned cleaning procedure, showing no significant difference. In the case of pure ethanol, $\theta_e = 0$ due to evaporation.

These measurements using a flat surface were found to be consistent with those exhibited by the particles in the experiments. For example, the equilibrium contact angle of the cleaned particles with a water droplet were $\theta_e \approx 30°$. To render the particles hydrophobic, as in liquid marble formation,[15] the beads were further subject to coating with a commercial hydrophobization agent (Glaco mirror coat zero, Soft 99 Co., Japan). In the case of water, this lead to an increase in equilibrium contact angle to $\theta_e \approx 110° \pm 20°$.

The snap-in process is captured by a high-speed video camera (Phantom V1611, Vision Research Inc.) equipped with objective lenses up to 20× at frame rates up to 100 000 fps. Depending upon the frame rate used the effective sensor resolution is from 1280 × 800 px down to 384 × 256 px, and we locate the moment of first contact accurate to within ±10–100 μs. The effective pixel size under the magnifications used is between 1.9 μm per px and 4 μm per px, meaning that the locations of the contact line are subject to a spatial resolution of up to ±8 μm. The videos are

Table 1 Physical properties of the test liquids. All concentrations are in %$_{w/w}$. The equilibrium contact angles stated are for glass surfaces cleaned as per the protocol described in the main text

Liquid	Density ρ (kg m^{-3})	Viscosity μ (mPa s)	Surface tension σ (mN m^{-1})	Equilibrium contact angle θ_e (deg)
Water	1000	1	72	34.2 ± 5.5
Glycerol (55.6%)	1130	8	67	40.2 ± 8.6
Ethanol (44.1%)	895	0.9	29.8	22.74 ± 3.2
Ethanol (100%)	789	1.19	23.2	0
NaCl (29%)	1187	1.4	80	42.6 ± 7.6
SDS (3%)	1000	1	30	16.1 ± 3.5

saved to a computer for subsequent analysis, which involved applying a custom-written routine in MatLab to extract the contact line position and contact angle, shown graphically in Fig. 2(b). The contact line position is specified by the arc angle ϕ from the top of the particle, whilst the contact angle θ is calculated as the angle between the tangents to the particle surface and the liquid interface at the contact line using a method similar to that presented in ref. 37.

Side-view measurements are known to significantly over-estimate the wetted radius at short times where its value is

$O(100~\mu\text{m})^{32}$ and this has lead to the reporting of an initial plateau in the wetted radius.[30] Therefore, only data points from the first frame before motion commences will be accepted to ensure that this false plateau does not interfere with the assessment of the evolution of the contact line.

3 Results and discussion

The results section is arranged as follows. First of all a qualitative overview of the snap-in process is given before the early wetting and lift-off stages are analyzed separately. We provide quantitative measurements of the evolution of the contact line, dynamic contact angle, θ, and equilibrium position for dense particles ($\rho_p/\rho = 2.11$–3.17) over a range of drop-to-particle diameter ratios ($R/r_p = 1.25$–15), whilst the lift-off stage is reconciled by a simple force balance.

3.1   Qualitative overview

An overview of the general snap-in process is shown in Fig. 1, whilst a close-up view of the very first motions is presented in Fig. 3 (see also the supplemental movie to accompany these figures, ESI†). From these images we can specify the stages of the process as follows: (i) early-time wetting stage, (ii) lift-off stage, where the particle leaves the substrate and attaches to the liquid interface, and (iii) approach to the equilibrium stage with oscillatory behavior. The early-time wetting is a relatively fast process with the contact line advancing at an average speed of 0.54 m s^{-1} over the first 500 μs. This speed is comparable to those reported in the data of ref. 30 for hydrophilic surfaces with $\theta_e = 3°$. Accompanying the contact line motion, a capillary wave with phase speed of approximately 1.09 m s^{-1} is observed to travel away from the contact line up around the drop. The lift-off occurs at $t^* \approx 4$ ms after first contact. At this point, the contact line has advanced by an arc length, $r\phi^* = 0.453$ mm, and the contact angle is $\theta^* = 82.5°$, where an asterisk denotes the value of a variable at lift-off.

Fig. 4 illustrates the effect of fluid properties, showing comparable sequences for four different liquids – namely – water, water–glycerol, water–ethanol and pure ethanol. In each trial, the particle size is the same and has been cleaned with the same procedure as outlined in Section 2. The primary qualitative differences between these representative images lie in the shape of the liquid interface during the lift-off stage ($t = 500$–700 μs) and the final location of the particle in equilibrium. Note that the particle becomes completely entrained into the ethanol droplet, indicating that the ethanol has perfectly wet the particle. With reference to Fig. 2(c), the balance between particle weight and capillary force from surface tension leads to a small protrusion at equilibrium for all liquids except ethanol. The raw data for the evolution of the contact line, in the form of wetted arc length $r\phi$ versus time, corresponding to the image sequences in Fig. 4(a) are plotted in Fig. 4(b). The data all exhibit the same trend, with a power-law type increase in $r\phi$ with t, i.e. $r\phi \propto t^\alpha$, until $t \approx 3$ ms (indicated by the vertical dash-dot line), which represents the crossover time from the

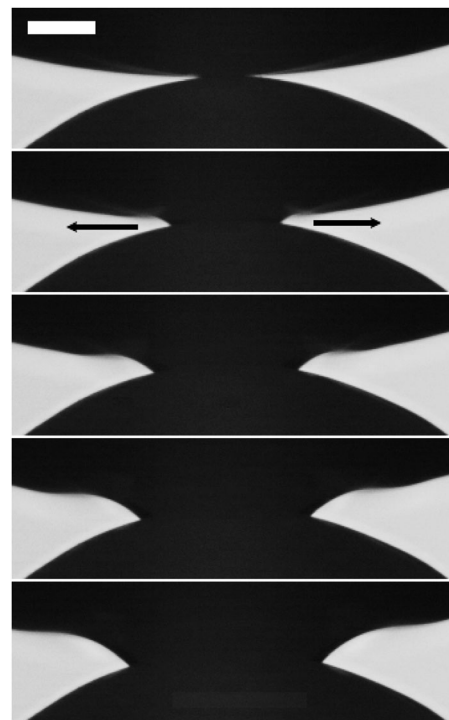Fig. 3   Image sequence showing the early-time evolution of the contact line of a pendant water droplet ($R = 2.7$ mm) along a glass bead with $r_p = 1$ mm. The scale bar in the first image is 100 μm long. Images are separated by 100 μs. The first image is the frame immediately prior to commencement of motion.

inertial regime to the viscous regime. The exact exponents of the power-law which provide the best-fit to the data in the inertial regime are $\alpha = 0.52$, 0.52, 0.51 and 0.55 for water, 55.6% glycerol, 44.1% ethanol and pure ethanol, respectively, whilst the constants of proportionality are all $O(10)$. Based on the results of ref. 30, we would expect to see a power-law exponent close to $1/2$ due to low equilibrium contact angles, $\theta_e \leq 30°$.

Fig. 5 shows a comparison between a hydrophilic and hydrophobic particle attaching to a water droplet. Some striking, yet intuitive, differences are observed here: firstly, for a given time, the contact line advances much further around the sphere in the case of the hydrophilic particle. Here, the lift-off stage occurs at approximately $t^* = 400$ μs, whereas the hydrophobic particle does not lift off until approximately $t^* = 800$ μs. Based upon the final (equilibrium) positions of these particles and the protrusion length, as shown in the final images at $t = 16$ ms, the equilibrium contact angles are estimated to be $\theta_e \approx 30°$ and $95°$ for the hydrophilic and hydrophobic particles, respectively.

The accompanying data extracted from image analysis for the wetted radius and contact angle versus time for the above realizations are shown in Fig. 6. In these plots, the same qualitative trends are observed for the evolution of the contact line as in Fig. 4(b), namely, a power-law progression of $r\phi$ in time until $t \approx 4$ ms, after which the dynamics exhibit a weaker dependence on time, as predicted by the transition to the viscous regime whereby $r \sim t^{1/10}$ (e.g. ref. 26). For the dynamic contact angle, Fig. 6(b) shows there is a rapid reduction during the very first motions with
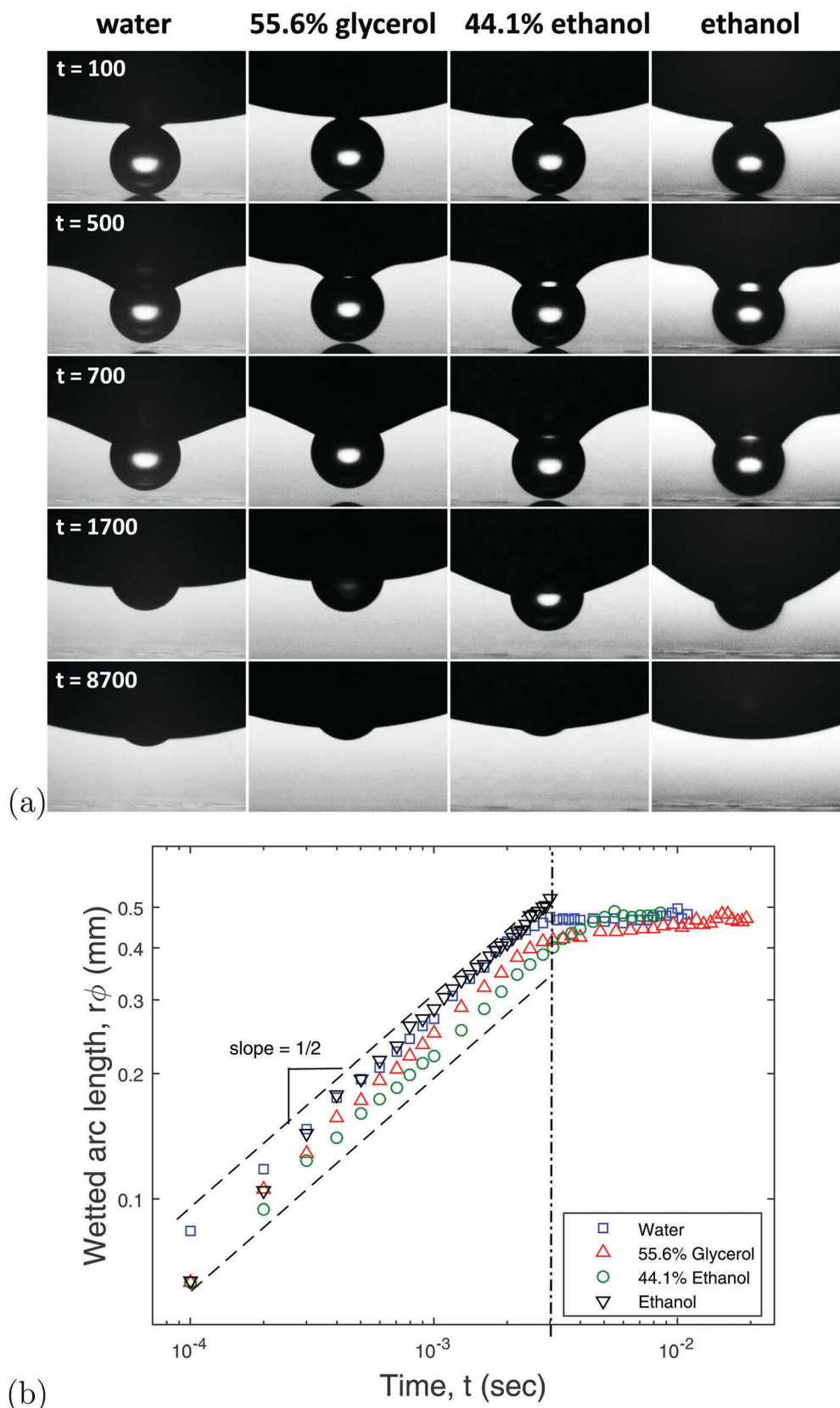
Fig. 4 (a) Comparison of snap-in effect for water, 55.6% glycerol, 44.1% ethanol and pure ethanol droplets with r_p = 198 μm and R/r_p = 13.57, 9.53, 9.75 and 8.02, respectively. The times in microseconds from first contact are indicated to the left. (b) Temporal evolution of the contact line around the particle, showing the wetted arc length, $r\phi$ vs. t, in a log–log plot. The dashed lines indicate a slope of 1/2, whilst the vertical dash-dot line at t = 3 ms indicates the approximate end of the inertial regime.
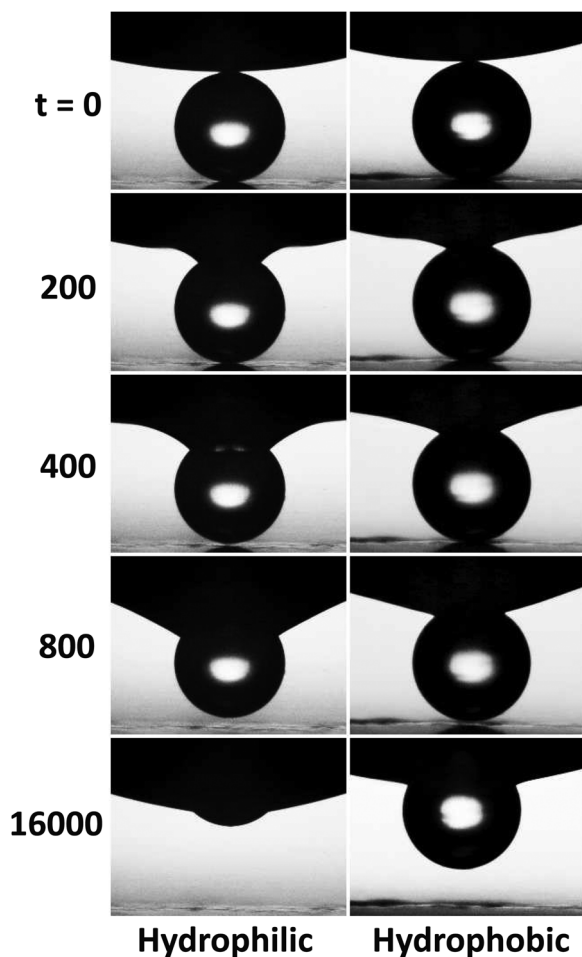
Fig. 5 Comparison between hydrophilic (r_p = 272 μm, R/r_p = 9.24) and hydrophobic (r_p = 268 μm, R/r_p = 8.13) particles attaching to a water drop. The times in microseconds from first contact are indicated to the left. See also the supplemental video accompanying this figure, ESI.†

θ decreasing from 180° to 100° within 300 μs for the hydrophilic particle, and from 180° to 130° over the same period for the hydrophobic particle. Following this initial rapid decay, there is a more modest decay in θ until $t \approx 4$ ms, coinciding with the transition to the viscous regime at which time the contact line advances more slowly. In the latter stages with $t \sim O(10^{-2})$, the particle oscillates about its equilibrium position, which is manifested by slight recession in the wetted arc length and increase in the contact angle. These oscillations arise due to the capillary waves between the particle and the glass tube but eventually decay to an equilibrium state (*e.g.* Fig. 2(c)).

3.2 Early wetting stage

To evaluate the early wetting stage, the correct length and time scales involved must be identified. In previous works for drops contacting flat substrates, the inertial and viscous timescales use the drop radius R as the lengthscale and $\tau_\sigma = (\rho R^3/\sigma)^{1/2}$ for the inertial-capillary timescale and $\tau_\mu = \mu R/\sigma$ for the viscous timescale.[26,30] For the snap-in process, however, we propose the correct length scale to collapse the inertial regime should be the particle radius r_p. The liquid density in the above inertial-capillary timescale should also be replaced by the particle density to give $\tau_p = (\rho_p r_p^3/\sigma)^{1/2}$.

This becomes obvious when the crossover time for the transition between the inertial and viscous regimes is evaluated. The crossover time can be derived by equating the radius of the contact line in both the inertial spreading regime $r^2 \sim \left(\sqrt{\sigma L/\rho}\right) t$ and the viscous regime $r \sim L(\sigma t/(\mu L))^{1/10}$, where L is the appropriate lengthscale, to give,

$$\tau_{\text{cross}} \sim \left(\frac{\rho \sigma L}{\mu^2}\right)^{1/8} \sqrt{\frac{\rho L^3}{\sigma}}. \qquad (1)$$
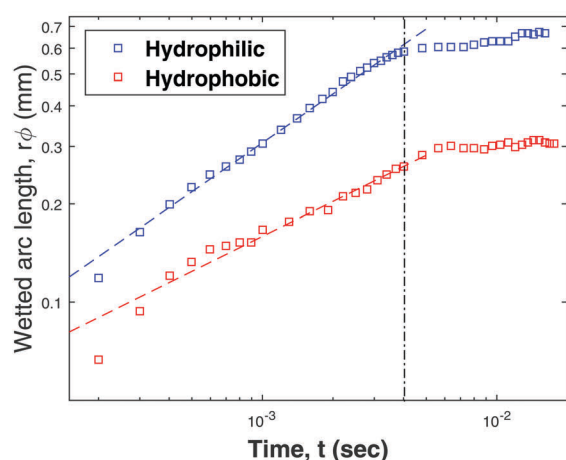
(a)
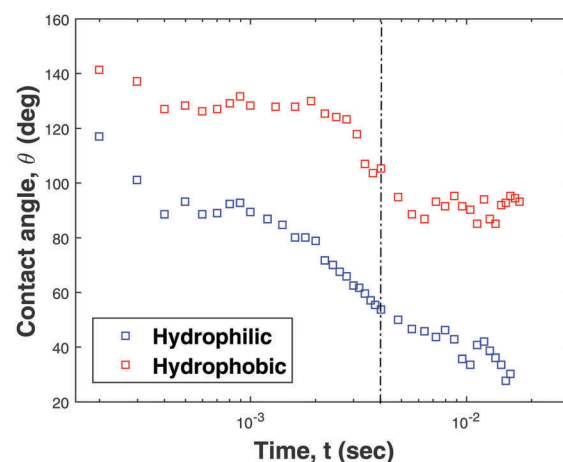
(b)

Fig. 6 Dynamics at the contact line from first contact for hydrophilic and hydrophobic particles corresponding to Fig. 5. The log–log plot (a) is of contact line position (wetted arc length) and (b) is of dynamic contact angle, both *versus* time. The vertical dashed lines indicates an apparent transition at $t \approx 4$ ms from inertial to viscous spreading regimes whilst the slopes in (a) indicate best power-law fits to the data with $r\phi = 9.67t^{0.499}$ and $r\phi = 1.86t^{0.36}$, respectively.
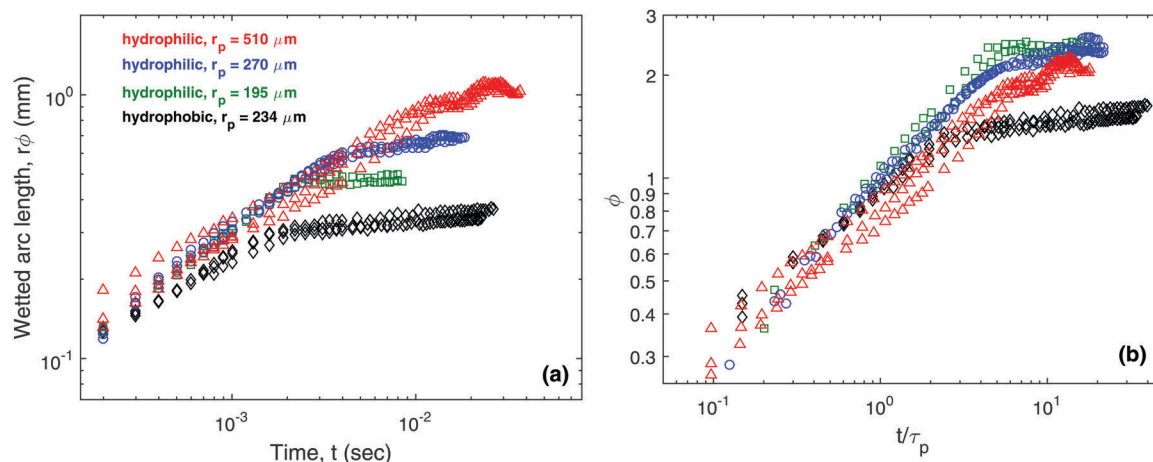
Fig. 7 Log–log plots of (a) wetted arc length, $r\phi$ versus time and (b) arc angle ϕ versus non-dimensional time, t/τ_p, for particles of various radius r_p in water.

By taking the drop radius as the lengthscale, *i.e.* $L = R$, the crossover times are $\tau_{cross} \approx 3 \times 10^{-2}$–$7 \times 10^{-2}$ s, which is clearly an order of magnitude above the actual crossover times as shown in Fig. 4(b) and 6(a). On the other hand, by setting $L = r_p$ and $\rho = \rho_p$, the crossover times $\tau_{cross} \approx 1.2 \times 10^{-3}$–$3.2 \times 10^{-3}$ s, in good quantitative agreement with the transition observed experimentally thus confirming the choice of particle radius and particle density as the correct length scale and density.

An example of raw and scaled data is presented in Fig. 7 with various particle radii in water. Whilst there is clear distinction between the hydrophilic and hydrophobic particles, we find that the scaled data, plotted as ϕ *vs.* t/τ_p largely collapse the data. However, as the particle size and liquid properties are varied, there are subtle differences in the slopes for the early-time data, *i.e.* $t \leq \tau_{cross}$. A previous approach[30] is now followed to assess the full range of the data presented here. For $t \leq \tau_{cross}$, the normalized data is fitted to the following power law model,

$$\phi = C(t/\tau_p)^\alpha. \qquad (2)$$

The results of this analysis are shown in Fig. 8(a) and (b), where the exponent α and prefactor C are found to both exhibit an inverse correlation with the equilibrium contact angle θ_e. The same dependence on θ_e was reported previously[30] and was explained by considering a balance of kinetic and surface energies leading to the conclusion that a relationship between the power-law exponent and equilibrium contact angle exists in the form $\alpha = C_1\sqrt{f(\theta_e) + \cos\theta_e}$. This would imply that α is solely dependent on θ_e. From our data, a weak dependence on the ratio of curvatures, R/r_p is also observed as shown in Fig. 8(c). However, given the significant amount of scatter in the data, we cannot draw a firm conclusion or explain this dependence. We note that the data for the lowest viscosity and lowest surface tension liquids (*e.g.* 44.1% ethanol and 3% SDS solutions) and those with the lowest contact angles ($\theta_e \approx 10$–$30°$) display a prefactor $C = 1.07$–1.25, in good quantitative agreement with the values $C \approx 1.11$–1.25 derived for coalescence.[29,38] As such, we conclude that the early-time wetting of curved liquid surfaces exhibits a power-law behavior controlled primarily by the equilibrium contact angle.

3.3 Lift-off stage

The lift-off stage commences once the particle first leaves the substrate it is sitting on. Subsequently, the particle moves vertically upwards towards the pendant droplet and undergoes several oscillations due to capillary waves traveling between the contact line on the sphere and the periphery of the pendant droplet, which is typically pinned to the outer diameter of the glass tube. The lift-off stage is expected to broadly coincide with the end of the inertial regime, since the timescale $\tau_p = (\rho_p r_p^3/\sigma)^{1/2}$, which can be deduced by balancing the rate of change of momentum, $\sim \rho_p r_p^4/\tau^2$, with the capillary force, $\sim \sigma r_p$. Fig. 9 indicates that this indeed the case with approximate agreement between the experimentally determined lift-off time, t_l, and τ_p.

As a first approximation to the motion of a particle attaching to a liquid interface, we consider a force balance taking into account particle weight, particle momentum and capillary forces all resolved in the vertical direction. However, we also postulate that the secondary effect of surface tension *via* Laplace pressure must also be taken into consideration, as seen previously.[39] With reference to Fig. 10, the contribution from the Laplace pressure acting during the early wetting and lift-off stage is approximated as

$$F_{\Delta P} \approx \sigma\left(\frac{1}{r_n} - \frac{1}{r_p\sin(\phi(t))}\right)\pi\left[r_p\sin(\phi(t))\right]^2, \qquad (3)$$

where r_n is the local radius of curvature shown in Fig. 10. Noting the sign of curvature of r_n relative to the direction of motion, this term is added to the capillary force arising from the contact line. However, this sign changes as the contact line advances further around the particle. Thus the total force balance is given by

$$F_{\sigma,z} + F_{\Delta P} - F_g = m\frac{\mathrm{d}v_p}{\mathrm{d}t}, \qquad (4)$$

where v_p is the instantaneous vertical particle speed and the terms $F_{\sigma,z}$ and F_g represent the vertical capillary force and weight given respectively by

$$F_{\sigma,z} = 2\pi r_p\sigma\sin(\phi(t))\sin(\theta(t) + \phi(t)), \qquad (5)$$
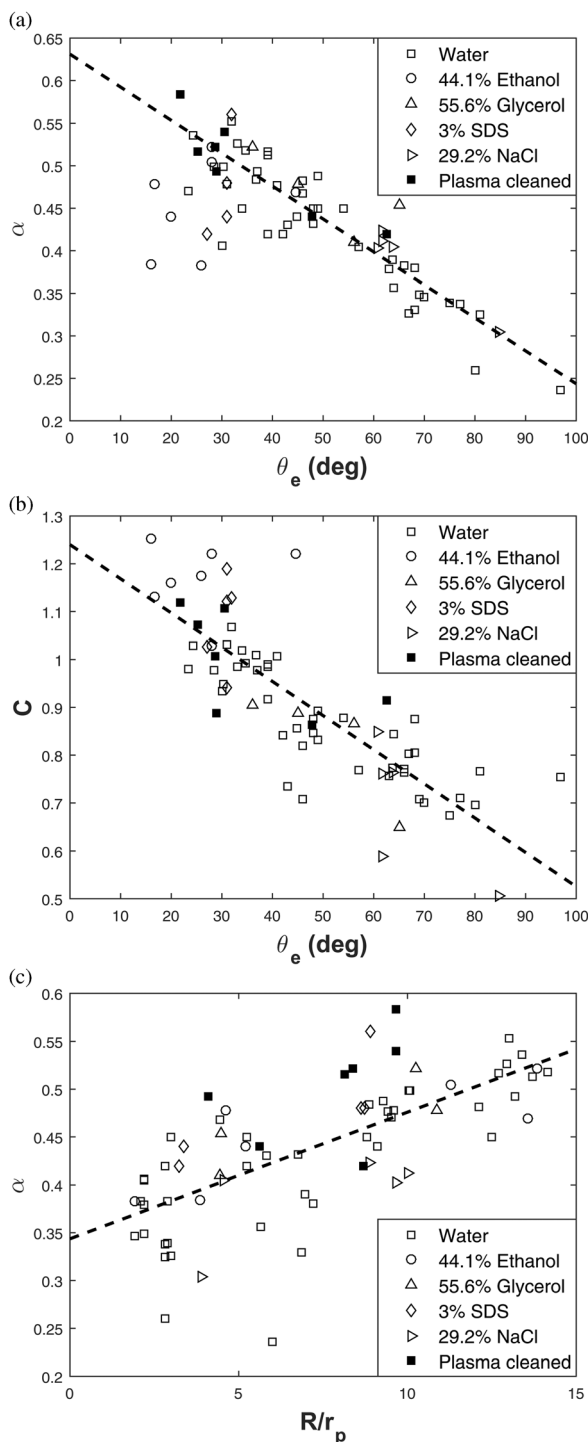
(a)

(b)

(c)

Fig. 8 Early-time spreading dynamics fitted to power law model $\phi = C(t/\tau_p)^\alpha$. Plots demonstrate the dependence of (a) the exponent α and (b) the constant prefactor C on equilibrium contact angle θ_e for the different liquids. (c) Power law exponent α versus curvature ratio R/r_p.

$$F_g = \frac{4}{3}\pi r_p^3 \rho_p g. \tag{6}$$

Eqn (4) can thus be solved and compared to experimental data for the height of the particle center. Fig. 11 presents example comparisons for plasma-cleaned glass beads attaching to a
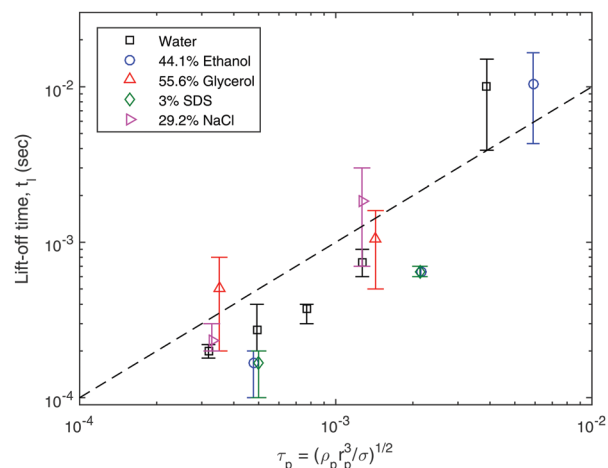

Fig. 9 A log–log plot of the experimental lift-off time, t_l, against the inertial timescale, $\tau_p = (\rho_p r_p^3/\sigma)^{1/2}$.
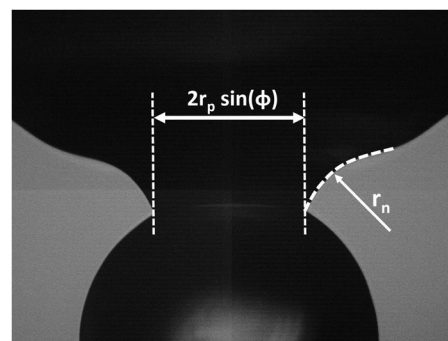

Fig. 10 Graphical illustration of interfacial curvature giving rise to a Laplace pressure component acting during the early wetting and lift-off stage.

water drop with $r_p = 510$ μm and $r_p = 207$ μm. In these examples, $t = 0$ indicates the first frame where liquid physically contacts the particle, and so we observe that the particle does not lift-off until $t \approx 1$ ms and $t \approx 300$ μs, respectively. At this point, the solution to eqn (4) without Laplace pressure (dashed line) departs from the experimental data and significantly over-estimates the extent of the displacement. However, the solution to eqn (4) with Laplace pressure, approximated by $F_{\Delta P}$ in eqn (3), provides excellent agreement with the measured particle displacement, thus justifying the inclusion of this term.[39]

At the moment of lift-off, just prior to particle motion, the particle has zero momentum ($v_p = 0$) and thus the weight of the particle, F_g, must balance with the capillary forces, $F_{\sigma,z}$, and the Laplace pressure differential term, $F_{\Delta P}$. Hence, eqn (4) at the moment of lift-off is given by

$$\frac{4}{3}\pi r_p^3 \rho_p g = 2\pi r_p \sigma \sin(\phi^*)\sin(\theta^* + \phi^*)$$
$$+ \left(\frac{1}{r_n} - \frac{1}{r_p \sin(\phi^*)}\right)\pi\left[r_p \sin(\phi^*)\right]^2, \tag{7}$$

where ϕ^* and θ^* indicate the arc angle and contact angle at the moment of lift-off. Performing this measurement over a range
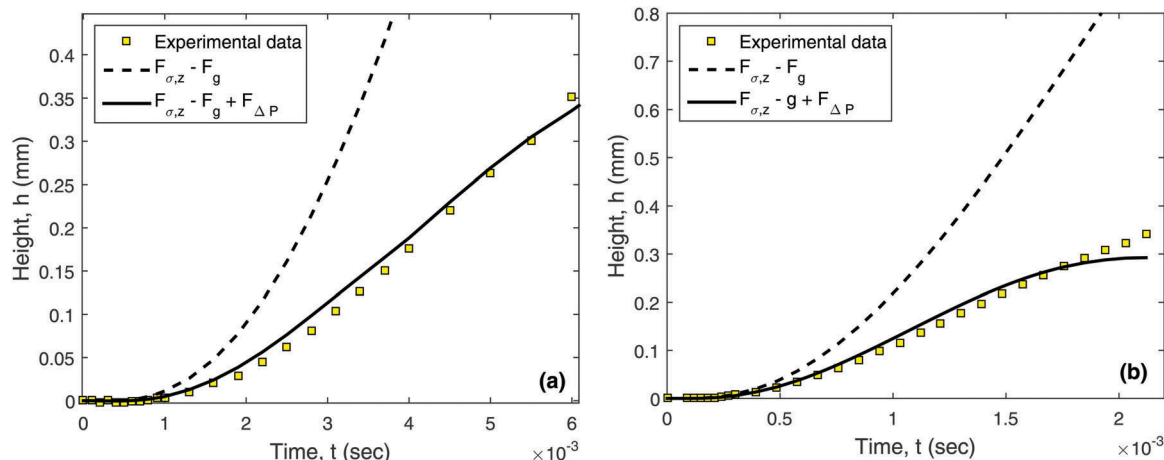
Fig. 11 Plots of particle center height, $h(t)$, *versus* time from contact, t for (a) r_p = 510 μm and (b) r_p = 207 μm and a water drop. The symbols represent data extracted from images. The dashed line represents the solution to eqn (4) with $F_{\Delta P} = 0$, whilst the solid line represents the solution to eqn (4), with $F_{\Delta P}$ given by eqn (3).

of fluids and particle sizes yields the results seen in Fig. 12(a). A discrepancy is observed between the two corresponding forces, $F_{\sigma,z} + F_{\Delta P}$, and F_g. In particular, the values of $F_{\sigma,z} + F_{\Delta P}$ overestimate the force needed to overcome the weight of the particle for the smallest particles, where for most of the data $F_{\sigma,z} + F_{\Delta P} = O(10^{-6})$ but $F_g = O(10^{-5})$. We attribute this overestimation to the limited spatial and temporal resolution (±8 μm, ±10–100 μs) of our particle tracking routine in that small accelerations will go unnoticed because there will be non-zero displacements at the sub-pixel level, which cannot be detected. For larger particles, where the contact line needs to advance farther around the particle before lift-off and with more pixels available for the tracking routine, this error diminishes and we observe good agreement, where $F_{\sigma,z} + F_{\Delta P} = F_g \approx 100$ μN with $r_p = 1$–1.1 mm. To provide a direct comparison between hydrophilic and hydrophobic particles, Fig. 12(b) shows the dependence of the mean lift off force against particle radius for water droplets. In contrast to ref. 18, we do not observe any quantifiable difference between the hydrophobic and hydrophilic particles. We also

note that there is considerable statistical noise in the data, evidenced by the large error bars, which we presume is due to a confluence of both microscopic liquid bridges between the particles and the substrate (*e.g.* ref. 25) and the temporal resolution limits.

The snap-in forces, F_s, reported in ref. 18 were measured at the first time that the particle crosses the equilibrium height and were derived from Hooke's law, $F_s = kD$, where k is the cantilever spring constant and D is the cantilever deflection. This gave snap-in forces of $O(10^{-6})$ N, whilst the weight of the particles used in their study are $O(10^{-10}$–$10^{-8})$ N for particle radii of $r_p = 20$–80 μm, showing that the snap-in force is far in excess of the particle weight. It would thus be insightful to extend the technique of ref. 18 to a larger range of particle radii to examine not only the snap-in force, but also the lift-off force, when the particle is first observed to move towards the liquid interface. We propose that this could resolve the discrepancy in our data in Fig. 12(a) and would require a combination of sensitive force measurement, such as in atomic force microscopy (AFM) coupled
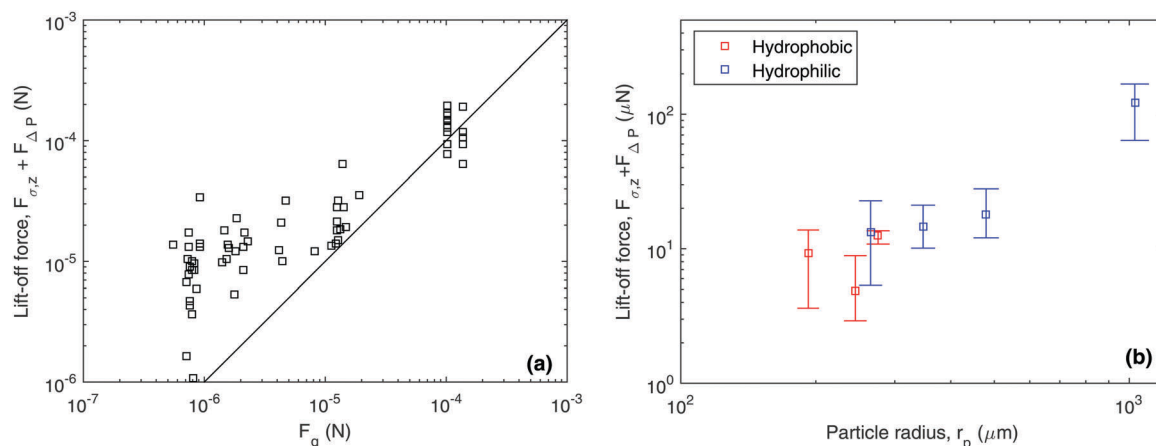
Fig. 12 Log–log plots for the comparison of forces at the moment of lift-off observed in the experiments. (a) Capillary and Laplace pressure forces *versus* particle weight for various liquids, and (b) mean lift-off force *versus* particle radius for water droplets only.

with ultra-high-speed video microscopy, with temporal resolution on the order of 1–10 μs, which is out of the scope of the present study, but will be addressed in future work.

Finally, we note that the typical force of a liquid droplet with radius of 1 mm and impact speed 3 m s^{-1} is approximately 50 mN,[40] which means that a droplet impacting a bed of loose particles will easily impart sufficient force to embed particles in the free-surface, even for hydrophobic particles with $\theta_e \approx 110° \pm 20°$, thus explaining the ease of liquid marble formation.

4 Conclusions

An experimental investigation was conducted into the attachment of particles to pendant liquid droplets, a process that is fundamental to the formation of a particle-laden interface. The three main stages were: (i) early-time wetting, (ii) particle lift-off, and (iii) approach to equilibrium and oscillation.

In the early wetting stage, we found that the advancement of the contact line is inertia-dominated and could be adequately described by the dimensionless power-law relationship $\phi = C(t/\tau_p)^\alpha$, where the characteristic lengthscale is the particle radius, r_p and the timescale is $\tau_p = (\rho_p r_p^3/\sigma)^{1/2}$. In accordance with the work of ref. 30, we found that the prefactor $C = O(1)$ and that both C and α are decreasing functions of the equilibrium contact angle. In particular, we observed that $\alpha \approx 0.5$ for water, where $\theta_e \approx 20–30°$, thus recovering the scaling law for inviscid coalescence. A less well-defined dependence on the curvature ratio, R/r_p, was also observed thus indicating that curvature does not play a significant role in this early wetting stage.

The particle lift-off stage was evaluated by matching the particle weight with both capillary force at the contact line and the Laplace pressure differential from local curvature effects. We observed that this simple force balance provided good agreement for the largest particles ($r_p \approx 1$ mm, $F_g = 100$ μN), but poor agreement for the smallest particles ($r_p \approx 200$ μm, $F_g \approx 1$ μN). We attribute this discrepancy to insufficient temporal and spatial resolution in that very small displacements occurred at sub-pixel levels that went undetected. We propose that this discrepancy could be resolved with ultra-high-speed microscopy coupled with sensitive force measurement. Finally, we did not observe any quantifiable trend in the lift-off force between hydrophobic and hydrophilic particles for the range of radii tested herein.

Future advances of this study will include repeating the experiments with multiple particles and a wider range of droplet curvatures. We will also address buoyancy effects by varying particle density. Furthermore, expanding the current parameter space to assess large droplet-to-particle diameter ratios as well as the influence of ambient humidity will be explored.

References

1 N. Pike, D. Richard, W. Foster and L. Mahadevan, How aphids roll their marbles, *Proc. R. Soc. B*, 2002, **269**, 1211–1215.

2 D. Quere and P. Aussillous, Non-stick droplets, *Chem. Eng. Technol.*, 2002, **25**, 925–928.

3 P. Aussillous and D. Quere, Properties of liquid marbles, *Proc. R. Soc. A*, 2006, **462**, 973–999.

4 B. P. Binks, Particles as surfactants – similarities and differences, *Curr. Opin. Colloid Interface Sci.*, 2002, **7**, 21–41.

5 G. G. Fuller and J. Vermant, Complex Fluid-Fluid Interfaces: Rheology and Structure, *Annu. Rev. Chem. Biomol. Eng.*, 2012, **3**, 519–543.

6 C. Monteux, E. Jung and G. G. Fuller, Mechanical properties and structure of particle coated interfaces: Influence of particle size and bidisperse 2D suspensions, *Langmuir*, 2007, **23**, 3975–3980.

7 D. Vella, P. Aussillous and L. Mahadevan, Elasticity of an interfacial particle raft, *Europhys. Lett.*, 2004, **68**, 212–218.

8 S. Barman and G. F. Christopher, Simultaneous Interfacial Rheology and Microstructure Measurement of Densely Aggregated Particle Laden Interfaces Using a Modified Double Wall Ring Interfacial Rheometer, *Langmuir*, 2014, **30**, 9752–9760.

9 P. Aussillous and D. Quere, Liquid marbles, *Appl. Opt.*, 2001, **411**, 924–927.

10 E. Bormashenko, Liquid marbles: properties and applications, *Curr. Opin. Colloid Interface Sci.*, 2011, **16**(4), 266–271.

11 E. Bormashenko and Y. Bormashenko, Non-stick droplet surgery with a superhydrophobic scalpel, *Langmuir*, 2011, **27**, 3266–3270.

12 P. S. Bhosale and M. V. Panchagnula, Sweating liquid micromarbles: Dropwise condensation on hydrophobic nanoparticulate materials, *Langmuir*, 2012, **28**, 14860–14866.

13 J. O. Marston, Y. Zhu, I. U. Vakarelski and S. T. Thoroddsen, Deformed liquid marbles: Freezing drop oscillations with powders, *Powder Technol.*, 2012, **228**, 424–428.

14 J. O. Marston, Y. Zhu, I. U. Vakarelski and S. T. Thoroddsen, Freezing drops with powders, *Phys. Fluids*, 2013, **25**, 091107.

15 T. Supakar, M. Moradiafrapoli, G. F. Christopher and J. O. Marston, Spreading, encapsulation and transition to arrested shapes during drop impact onto hydrophobic powders, *J. Colloid Interface Sci.*, 2016, **468**, 10–20.

16 M. Cui, T. Emrick and T. P. Russell, Stabilizing liquid drops in nonequilibrium shapes by the interfacial jamming of nanoparticles, *Science*, 2013, **342**, 460–463.

17 A. P. Kotula and S. L. Anna, Probing timescales for colloidal particle adsorption using slug bubbles in rectangular microchannels, *Soft Matter*, 2012, **8**, 10759–10772.

18 L. Chen, L.-O. Heim, D. S. Golovko and E. Bonaccurso, Snap-in dynamics of single particles to water drops, *Appl. Phys. Lett.*, 2012, **101**, 031601.

19 S. Cappelli, Q. Xie, J. Harting, A. M. de Jong and M. W. J. Prins, Dynamic wetting: status and prospective of single particle based experiments and simulations, *New Biotechnol.*, 2015, **32**, 420–432.

20 V. N. Manoharan, Pinned down, *Nat. Mater.*, 2015, **14**, 869–870.

21 T. Young, An essay on the cohesion of fluids, *Philos. Trans. R. Soc. London*, 1805, **95**, 65–87.

22 R. L. Hoffman, A study of the advancing interface. I. Interface shape in liquid–gas systems, *J. Colloid Interface Sci.*, 1975, **50**, 228–241.

23 T. D. Blake, The physics of moving contact lines, *J. Colloid Interface Sci.*, 2006, **299**, 1–13.

24 M. J. Neeson, D. Y. C. Chan and R. F. Tabor, Compound pendant drop tensiometry for interfacial tension measurement at zero Bond number, *Langmuir*, 2014, **30**, 15388–15391.

25 M. J. Neeson, R. Dagastine, D. Y. C. Chan and R. F. Tabor, Evaporation of a capillary bridge between a particle and a surface, *Soft Matter*, 2014, **10**, 8489–8499.

26 A.-L. Biance, C. Clanet and D. Quere, First steps in the spreading of a liquid droplet, *Phys. Rev. E: Stat., Nonlinear, Soft Matter Phys.*, 2004, **69**, 016301.

27 J. Eggers, J. R. Lister and H. A. Stone, Coalescence of liquid drops, *J. Fluid Mech.*, 1999, **401**, 293–310.

28 M. Wu, T. Cubaud and C.-M. Ho, Scaling law in liquid drop coalescence driven by surface tension, *Phys. Fluids*, 2004, **16**, L51–L54.

29 S. T. Thoroddsen, K. Takehara and T. G. Etoh, The coalescence speed of a pendant and a sessile drop, *J. Fluid Mech.*, 2005, **527**, 85–114.

30 J. C. Bird, S. Mandre and H. A. Stone, Short-time dynamics of partial wetting, *Phys. Rev. Lett.*, 2008, **100**, 234501.

31 K. G. Winkels, J. H. Weijs, A. Eddi and J. H. Snoeijer, Initial spreading of low-viscosity drops on partially wetting surfaces, *Phys. Rev. E: Stat., Nonlinear, Soft Matter Phys.*, 2012, **85**, 055301(R).

32 A. Eddi, K. G. Winkels and J. H. Snoeijer, Short time dynamics of viscous drop spreading, *Phys. Fluids*, 2013, **25**, 013102.

33 B. B. J. Stapelbroek, H. P. Jansen, E. S. Kooij, J. H. Snoeijer and A. Eddi, Universal spreading of water drops on complex surfaces, *Soft Matter*, 2014, **10**, 2641–2648.

34 F. M. Orr, L. E. Scriven and A. P. Rivas, Pendular rings between solids: meniscus properties and capillary force, *J. Fluid Mech.*, 1975, **67**, 723–742.

35 M. Guilizzoni, Drop shape visualization and contact angle measurement on curved surfaces, *J. Colloid Interface Sci.*, 2011, **364**, 230–236.

36 C. W. Extand and S. I. Moon, Contact angle on spherical surfaces, *Langmuir*, 2008, **24**, 9470–9473.

37 D. Biole and V. Bertola, A goniometric mask to measure contact angles from digital images of liquid drops, *Colloids Surf., A*, 2015, **467**, 149–156.

38 D. G. A. L. Aarts, H. N. W. Lekkerkerker, H. Guo, G. H. Wegdam and D. Bonn, Hydrodynamics of droplet coalescence, *Phys. Rev. Lett.*, 2005, **95**, 164503.

39 J. Ally, E. Vittorias, A. Amirfazli, M. Kappl, E. Bonaccurso, C. E. McNamee and H.-J. Butt, Interaction of a microsphere with a solid-supported liquid film, *Langmuir*, 2010, **26**, 11797–11803.

40 D. Soto, A. B. De Lariviere, X. Boutillon, C. Clanet and D. Quere, The force of impacting rain, *Soft Matter*, 2014, **10**, 4929–4934.

41 Y. D. Shikhmurzaev, *Capillary Flows with Forming Interfaces*, Chapman & Hall/CRC, Boca Raton, 2007.